THE JOURNAL OF
PHYSICAL CHEMISTRY C

Article

Cite This: *J. Phys. Chem. C* 2017, 121, 23875–23885

pubs.acs.org/JPCC

First-Principles Study of Fluorescence in Silver Nanoclusters

Samuel L. Brown,[†] Erik K. Hobbie,[†] Sergei Tretiak,[‡] and Dmitri S. Kilin*[,§,†]

[†]Materials and Nanotechnology Program, North Dakota State University, Fargo, North Dakota 58108, United States
[‡]Center for Integrated Nanotechnologies, Los Alamos National Laboratory, Los Alamos, New Mexico 87544, United States
[§]Department of Chemistry and Biochemistry, North Dakota State University, Fargo, North Dakota 58108, United States

Supporting Information

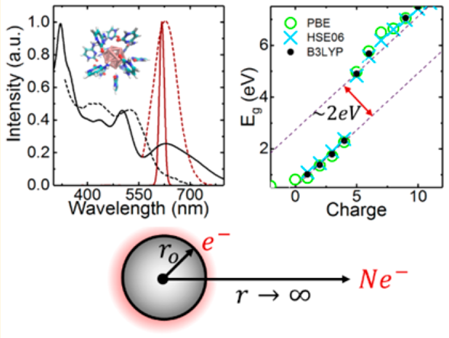

ABSTRACT: Mechanisms of efficient fluorescence from biocompatible, ligand-protected silver nanoclusters (AgNC) are explored with an atomistic model of an icosahedral shaped AgNC passivated with 12 cytosine molecules representing single-stranded DNA. Spin-resolved density-functional theory with varying constraints to the total charge was used as a simulation probe to explore the electronic structure and photoluminescence of AgNCs. Visible photoemission in AgNCs is modeled through a synergy of radiative and nonradiative photoinduced dynamics computed by a combination of density matrix and density functional methods with explicit treatment of spin polarization. The ab initio computed charge-to-total energy correlation, $E_{\mathrm{tot}}(\Delta N)$, of the modeled AgNC shows an approximate 2.2 eV discontinuity at a charge of $\Delta N = 5$, which correlates with the DFT calculated band gap and with concept of superatom with closed shell valence electron count [*PNAS* **2008**, *105*, 9157]. UV photoexcitation of this cationic model followed by cascade thermalizations toward the band edges is modeled using Redfield theory, and the corresponding time-integrated emission is calculated. Peak emission near 610 nm is found, consistent with experimentally reported PL in AgNCs. This work gives further insight into the recombination kinetics of AgNC and can be used to aid in tailoring their optical properties to maximize fluorescence efficiency and tunability.

1. INTRODUCTION

Photoluminescent silver nanoclusters (AgNCs) are ideally suited for biological applications, being the "Goldilocks" of fluorophores with just the right size, level of toxicity, and photostability.[1] Biological applications requiring fluorophores, such as biolabels and biosensors, typically use either organic dyes or metal-chalcogenide quantum dots. In these applications, quantum dots offer superior photostability when compared to organic dyes, yet consist primarily of toxic materials such as lead and cadmium.[2−6] Aside from the toxicities, quantum dots are typically large and cumbersome for transport through biological membranes.[1,7,8] AgNCs on the other hand, with core diameters of 1 nm or less, can be readily transported throughout the body, while the relatively benign nature of silver addresses potential concerns about nanotoxicity.[9−17] Furthermore, AgNCs have demonstrated highly efficient photoemission with quantum yields as high as 90% in some cases.[18]

These highly efficient AgNCs are typically synthesized using DNA to limit large nanoparticle growth and maintain stability.[18−23] The biocompatibility of DNA and AgNCs gives researchers the ability to employ their photoluminescent properties in various biobased applications. For instance, Yu et al. were able to take in vitro cell images of fluorescent silver nanocluster markers[24] while Yeh and co-workers created AgNC sensors by leveraging the sensitivity of the AgNC's optical properties to the nanocluster environment/surface.[25] The sensitivity of AgNC optical properties to the surrounding environment is well established.[21,25−27] Note that simplified mono-orbital description of excited states precludes us to clearly treat the orbital relaxation effects in each multiplicity case but provides a uniform interpretative comparison across all charge scenarios. In one example, Diez et al. showed that systematic decreases in the solvating water to methanol ratio of polymer stabilized AgNCs resulted in a bathochromic shift in the photoluminescence (PL).[26] In accord with surface sensitivity, Richards and co-workers used combinatorial chemistry to demonstrate that, by simply changing the DNA sequence used to stabilize the nanoparticles, PL spanning the entire visible spectrum can be achieved.[21] This work was then expanded upon by the Gwinn group, who used random DNA oligomers to synthesize more than 600 different AgNC complexes.[20] A Gaussian was used to fit the measured emission spectra of each sample and a corresponding histogram was developed for the peak emission. Of the emission peaks measured, most DNA/AgNC complexes exhibited peak PL emission at either 540 or 630 nm. Deemed as magic colors, the Gwinn group proposed that this was due to the AgNCs predominantly adopting a structure corresponding to a magic number.[20]

Received: May 19, 2017
Revised: August 4, 2017
Published: September 19, 2017

ACS Publications

DOI: 10.1021/acs.jpcc.7b04870

Furthermore, mass spectroscopy findings by several groups indicate that fluorescent AgNCs are highly charged, having a charge of 4+ or greater depending on size.[18,22,28,29] Alongside this, the high charge has been hypothesized to be due to Ag^+ atoms surrounding a neutral $Ag^{(0)}$ core,[18,28] much like that of superatom complexes.[30]

We start with detailing a new general methodology allowing spin-resolved PL to be modeled. In the present AgNCs case this approach is required to account for the open-shell nature of the valent d and s orbitals of silver. We then examine the electronic structure of AgNCs with different charges and ground-state (GS) spin configurations to identify promising scenarios with a high potential for fluorescence (i.e., the presence of a band gap). The PL of one of these models (singlet 5+) is then calculated explicitly to exemplify emerging photophysics and to provide mechanistic insights.

Atomistic modeling of AgNCs, or more broadly noble metal nanoclusters, is generally developed in four main directions: (i) electronic structure as a function of morphology, (ii) optical absorption, (iii) excited state dynamics, and (iv) photoemission properties.

(i) General electronic structure calculations seek to establish correlations between the size, shape, and morphology of the nanocluster and its electronic structure features, such as the value of the HOMO−LUMO gap. The main challenge for this research direction originates from the large amount of iso-energetic isomers for a given number of atoms.[31] For instance, an atomistic modeling argument was recently used to debate whether the Ag−DNA structures are metallic or a metalorganic complex.[32] Alongside this, there are several atomistic investigations on the specific surface passivation of silver nanostructures.[33]

(ii) Simulations of the linear optical absorption of metallic nanoclusters are typically performed using a TDDFT methodology.[34−37] This methodology typically computes excited states of specific multiplicity from a reference ground state. While the TDDFT approach properly addresses the many-body nature of excited electronic states, such modeling is numerically costly and it is challenging to interpret the origin of spectral peaks[36,38] and to establish their connection to the plasmonic spectral features typical of larger metallic nanostructures.[39] As a first step here we stay with simplified mono-orbital description of excited states allowing for direct intuitive interpretation and reduced computational cost.

(iii) Atomistic calculations of excited state dynamics offer detailed information on dynamical processes in metal clusters following photoexcitation. Excited state dynamics in general[40] can be modeled by a method of survival probability,[41,42] multiple spawning,[43−45] surface hopping,[37,46] or density matrix.[47] For AgNCs dynamics, interesting results were recently reported in the ultrafast time domain by FDTD and RT-TDDFT[48] and for the intermediate-to-long time domain.[49] Modeling of extended times on the order of 1 ps exhibits processes such as phonon-induced dissipation, relaxation, and charge transfer[50] between a metal cluster and a semiconductor substrate.[51,52] One of the practical challenges in modeling the relaxation dynamics of metallic nanoparticle systems comes from the open shell nature of the d and s valent orbitals in transition metals. However, one can circumvent this issue by assuming independent relaxation in each of the two different spin components, alpha and beta.[53,54]

(iv) The fourth research direction is atomistic modeling of photoemission, which is still in its infancy due to technical challenges. Specifically, photoemission cannot be simulated as a standalone electronic process. It is a synergy of radiative and nonradiative electronic transitions that drastically depends on the excited states' lifetimes. Moderate progress has been recently achieved in modeling the PL of semiconductor nanostructures, such as titania and silicon.[55−57] Specifically, Vogel et al. showed that insight from room temperature molecular dynamics (MD) simulations coupled with the application of the Redfield master equation to the Fourier transform of nonadiabatic couplings can be used to calculate time dependent and steady state PL in nanostructures.[56] Similarly, Meng and co-workers modeled the photoemission of thiolate-protected gold nanoclusters using similar methodologies.[58]

The remainder of this paper is organized as follows: An overview of the methodology is given in section 2, with subsection 2.1 focusing on the general aspects of spin resolved electronic structure, subsection 2.2 focusing on electron dynamics and photoemission, and subsection 2.3 providing practical computational details. Section 3 provides results on electronic structure and dynamics calculations for a specific AgNC model. Section 4 includes a discussion and provides an appealing interpretation of the results in comparison with intuitive expectations, classical electrostatics, and superatom concept. Finally, conclusions and outlook are summarized in section 5.

2. METHODOLOGY

2.1. Theoretical Approaches to Spin-Resolved Electronic Structure. Note that spin resolved calculations are important in this application of DFT due to the open shell nature of the d and s valent orbitals in the silver atoms forming a nanocluster. A simplified introduction of a spin-enabled DFT is given here for consistent notation and a coherent presentation. These notations for basic quantities are needed for the rigorous definition of the nontrivial approaches introduced in what follows and in the Supporting Information (SI). All electronic structure calculations were performed in a self-consistent manner using DFT[59] with spin resolved components and constraints[60] providing set of Kohn−Sham (KS) orbitals $\varphi_{i,\sigma}^{KS}(\vec{r})$ and energies of the KS orbitals $\varepsilon_{i,\sigma}$ with $\sigma = \alpha$ or β standing for different spin projections. The self-consistent DFT procedure is cast in terms of spin resolved electron densities, $\rho_\alpha(\vec{r}) = \Sigma_{i=1}^{N_\alpha}|\varphi_{i,\alpha}^{KS}|^2$ and $\rho_\beta(\vec{r}) = \Sigma_{i=1}^{N_\beta}|\varphi_{i,\beta}^{KS}|^2$, where N_α and N_β stand for the number electrons with alpha and beta spin projections, respectively. The DFT calculated electronic structure and total energy E^{tot} are conveniently parametrized by the total charge

$$N = N_\alpha + N_\beta \tag{1a}$$

and spin polarization[61,62]

$$\Delta N_{\uparrow\downarrow} = N_\alpha - N_\beta \tag{1b}$$

The value of the spin polarization parameter can be used to identify spin multiplicity as follows: 2S + 1, where $S = \Delta N_{\uparrow\downarrow}/2$. Thus, a progression of $\Delta N_{\uparrow\downarrow} = 0, 1, 2, 3, \ldots$ corresponds to singlet, doublet, triplet, quartet, ... multiplicities, respectively. For each pair of parameters N and $\Delta N_{\uparrow\downarrow}$, we analyze the spin resolved band gap

$$\Delta\varepsilon_\sigma^{gap}(N, \Delta N_{\uparrow\downarrow}) = \varepsilon_\sigma^{LU}(N, \Delta N_{\uparrow\downarrow}) - \varepsilon_\sigma^{HO}(N, \Delta N_{\uparrow\downarrow}) \tag{2a}$$

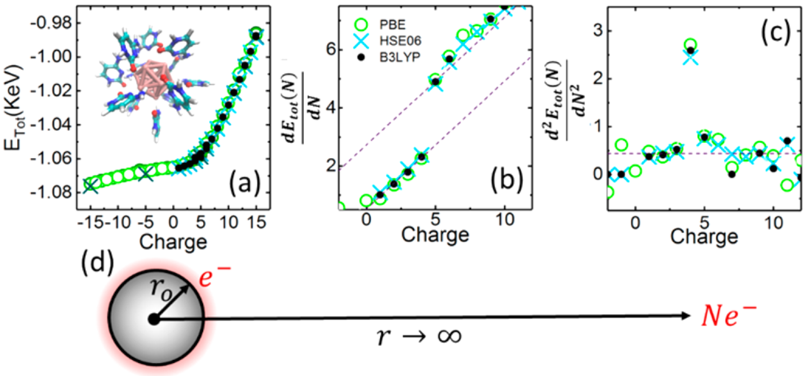

Figure 1. (a) Total energy as a function of charge for the modeled nanocluster (inset) with the corresponding (b) first and (c) second derivative. The purple dashed lines in (b) are linear fits of the form $\frac{\mathrm{d}E}{\mathrm{d}N} = A_1 + BN$ and $\frac{\mathrm{d}E}{\mathrm{d}N} = A_2 + BN$ such that $A_1 < A_2$. The jump discontinuity here represents a deviation from classic electrostatics as quantum mechanical effects become important. (d) Charge-constrained DFT was used for each calculation where an electron is removed the silver nanocluster. Green circle, blue cross, and black dot stand for PBE, HSE06, and B3LYP data, respectively.

as well as the change in total energy

$$\Delta E^{\mathrm{tot}}(N_\alpha, N_\beta) = E^{\mathrm{tot}}(N_\alpha + 1, N_\beta) - E^{\mathrm{tot}}(N_\alpha, N_\beta) \tag{2b}$$

where, in all calculations, the passivating ligands' electrons are included in N.

The calculated KS orbitals can be used to construct a Slater determinant and find the transition dipole expectation values, $\langle \vec{D}_{ij,\sigma} \rangle = e \int \varphi_{i\sigma}^* \vec{r} \varphi_{j\sigma} \, \mathrm{d}\vec{r}$, in the independent orbital approximation (IOA),[63] where e is the charge of an electron and $\vec{r}$ is the position operator. Here we note that the singly excited state is often described as a superposition of occupied and unoccupied molecular orbital pairs, e.g., as in solutions of the Bethe-Salpeter equation; $\Sigma_{i'j'} H_{iji'j'} A_{i'j'}^{\xi} = E^{\xi} A_{ij}$, with the many-electron Hamiltonian $H_{iji'j'} = (\varepsilon_i - \varepsilon_j)\delta_{ii'}\delta_{jj'} + W_{ii'jj'}$ in the basis of single electron orbitals $|i\rangle$ and $|j\rangle$ with Coulomb interactions, $W_{ii'jj'}$. The eigenstates are $|\xi\rangle = \Sigma_{ij} A_{ij}^{\xi} \, |i\rangle|j\rangle$ with normalization $\Sigma_{ij}|A_{ij}^{\xi}|^2 = 1$. A description of the dynamics requires a recalculation of these excited states $|\xi(t)\rangle$ and $A_{ij}^{\xi}(t)$ for nuclear configurations at each time along the trajectory. As an approximation, the superposition of states is represented by only the leading term as $A_{ij}^{\xi}(t) \approx \delta_{i,i'(\xi)} \cdot \delta_{j,j'(\xi)'} + ...$, where the excited state, ξ, is approximated as a pair of orbitals, occupied $i'(\xi)$ and unoccupied $j'(\xi)$, with both depending on ξ, which is referred to as the IOA.[63]

The transition dipole expectation values can then be used to find the oscillator strength of an electronic transition from KS orbital i to KS orbital j, with given spin σ, such that

$$f_{ij,\sigma} = |\vec{D}_{ij,\sigma}|^2 \frac{4\pi m_e \nu_{ij,\sigma}}{3\hbar e^2} \tag{3a}$$

where m_e is the mass of an electron. Using the oscillator strengths and assuming a lack of spin–orbit coupling, the absorption spectra can then be determined from eqs 3a, 3b, and 4.

$$\alpha_\sigma(\omega) = \sum_{ij} f_{ij,\sigma} \delta(\varepsilon - \Delta\varepsilon_{ij,\sigma}) \tag{3b}$$

$$a(\omega) = a_\alpha(\omega) + a_\beta(\omega) \tag{4}$$

2.2. Theoretical Approaches to Electron Dynamics and Photoemission. The existing literature on the ab initio computation of emission spectra for open shell configurations is limited, so the practical steps needed for the computation of spin-resolved emission are introduced for the first time in this work. Our approach is built on earlier developments for computing the emission of the closed shell structures, which have been previously noted.[52,55−57,64]

To calculate time-dependent spin-resolved PL, we expand upon a previously reported methodology for the calculation of time-dependent spin-unresolved PL.[56] This approach rests on the time propagation of the excited states, facilitated by energy dissipation into phonons. The methodology includes five stages of computation: thermostat modeling, molecular dynamics, nonadiabatic couplings, Redfield dissipative dynamics, and computation of photoemission. Briefly, one runs a room temperature adiabatic MD simulation on the silver nanocluster in which $\sum_{I=1}^{N^{\mathrm{ion}}} \frac{M_I}{2} \left(\frac{\mathrm{d}\vec{R}_I}{\mathrm{d}t} |_{t=0} \right)^2 = \frac{3}{2} N^{\mathrm{ion}} k_{\mathrm{B}} T$ is used as an initial condition for modeling a thermostat, where M_I and $\vec{R}_I$ are the mass and position of ion I, respectively, and N^{ion} is the total number of ions. Ion position changes as a function of time by Newton's equation of motion

$$\frac{\mathrm{d}^2}{\mathrm{d}t^2} \vec{R}_I = \vec{F}_I / M_I \tag{5}$$

which consequently alters the KS orbitals, giving $\varepsilon_{i,\sigma}(t) = \varepsilon_{i,\sigma}(\overrightarrow{R_I}(t))$. Nonadiabatic couplings (NACs) are determined "on-the-fly",[65] which are then used to determine the components of the Redfield tensor, R_{ijml}. The Redfield tensor and Fock matrix, $H_{ij,\sigma} = \delta_{ij}\varepsilon_{i\sigma}(t)$, are used in the Redfield master equation[47] (eq 6) to determine the orbital occupation as a function of time;

$$\dot{\rho}_{ij,\sigma} = \frac{i}{\hbar} \sum_k (H_{ik,\sigma}\rho_{kj,\sigma} - \rho_{jk,\sigma}H_{ki,\sigma}) + \sum_{lm} R_{ijml,\sigma}\rho_{lm,\sigma} \tag{6}$$

With an understanding of the spin-resolved orbital occupation $\rho_{ii,\sigma}$(t) as a function of time, one can calculate the time dependent and steady state PL using eqs 7, 8a, and 8b, respectively

$$E_\sigma(\omega, t) = \sum_{ij} f_{ij\sigma} \delta(\hbar\omega - \Delta\varepsilon_{ij\sigma})(\rho_{jj\sigma}(t) - \rho_{ii\sigma}(t)) \tag{7}$$

DOI: 10.1021/acs.jpcc.7b04870
J. Phys. Chem. C 2017, 121, 23875−23885

$$E_\sigma(\omega) = \int_0^\infty \mathrm{d}t\ E_\sigma(\omega, t) \tag{8a}$$

The summation of PL for both alpha and beta spins results in the total PL

$$E(\omega) = E_\alpha(\omega) + E_\beta(\omega) \tag{8b}$$

More details on the calculation of the PL are available in the SI.

2.3. Comutational Details. The AgNC modeled in this study is shown in the inset of Figure 1a. Small metal clusters exhibit a broad variety of isomers with multiple geometries yielding similar energies. Iterative scanning of the size and shape of the cluster is beyond the scope of this paper; instead, we focus purely on optimizing the electronic configuration in a selected high-symmetry cluster, Ag_{13}, which is a typical geometry for transition metal clusters.[36,66−68] It consists of 13 silver atoms in the icosahedral geometry with one central Ag atom and 12 surface shell silver atoms. Each surface silver atom is passivated by a cytosine base to represent DNA. This constitutes the simplest spherical cluster model. The chosen geometry is similar but not equal to the geometry determined experimentally by Petty.[28]

All electronic structure simulations were performed in the Vienna ab initio simulation package (VASP) suite with projector augmented wave (PAW) potentials.[69−72] The GS geometry of the modeled AgNC was optimized using DFT with the Perdew−Burke−Ernzerhof (PBE) functional.[71] For a reasonable range of cationic charges, the geometry did not experience qualitative changes upon optimization. Electronic wave functions were expanded in a plane wave basis set with a kinetic energy cutoff of 500 eV. The atoms in the unit cell are fully relaxed until the force on each atom is less than 0.01 eV/Å.

Spin-resolved DFT calculations were performed with one generalized gradient approximation (GGA) functional PBE and two hybrid functionals, namely Heyd-Scuseria-Ernzerhof (HSE06),[73] and Becke, 3-parameter, Lee−Yang−Parr (B3LYP)[74,75] exchange-correlation kernels. Periodic boundary conditions (PBC) are implemented with 8 Å of vacuum added in each direction to avoid spurious interactions. The spurious electrostatic interactions between replicas of charged species discussed by Neugebauer and Scheffler[76] are avoided with the use of a background charge concept, as suggested by Makov and Payne[77] and used for modeling of charged metal clusters in PBC.[78]

3. RESULTS

To begin our analysis, we examine the energy-charge space of the modeled AgNC. In Figure 1a the total energy as a function of cationic charge obtained by removing N electrons in respect to neutral model, $E_{\mathrm{tot}}(N)$, takes the general form of a quadratic function, consistent with the finding of Meng et al. for platinum nanoclusters.[79] A general method for evaluating the stability of a model relates to the calculated total energy. Higher energy systems are expected to be more unstable. Here we see little difference between the calculated total energies of different multiplicities well below the error margin for a given DFT methodology. Although it is possible that the sextet multiplicity would lead to a more stable complex due to the 5 nearly degenerate singly occupied d orbitals we did not examine this specific multiplicity.

Figure 1b,c shows the first $\left(\frac{\mathrm{d}E_{\mathrm{tot}}(N)}{\mathrm{d}N}\right)$ and second $\left(\frac{\mathrm{d}^2E_{\mathrm{tot}}(N)}{\mathrm{d}N^2}\right)$ derivative of $E_{\mathrm{tot}}(N)$ with respect to charge, which are expected to show a linear and constant dependence on N, respectively. Although we calculate the total energy for the singlet, doublet, triplet, and quartet GS configuration, we only use the singlet and doublet GS configurations to determine $\frac{\mathrm{d}E_{\mathrm{tot}}(N)}{\mathrm{d}N}$ and $\frac{\mathrm{d}^2E_{\mathrm{tot}}(N)}{\mathrm{d}N^2}$. The first derivative $\frac{\mathrm{d}E_{\mathrm{tot}}(N)}{\mathrm{d}N}$ exhibits a linear trend with a clear discontinuity present at a charge of 5+. These trends are fit with two lines per eq 9 below as illustrated in Figure 1b

$$\frac{\mathrm{d}E(N)}{\mathrm{d}N} - BN = \begin{cases} A_1, & N < 5 \\ A_2, & N > 5 \end{cases} \tag{9}$$

where B is the slope of the line and $A_{1,2}$ is a constant. Interestingly, on either side of the jump discontinuity, we see that the slope of the line does not change ($B \approx 0.439$) and the only difference is found between the two values of the constant ($\Delta A = A_2 - A_1 \approx 2.2$ eV). The derivative of eq 9, $\frac{\mathrm{d}^2E(N)}{\mathrm{d}N^2}$, is dependent only on the slope, B, which is applicable to the entire range excluding $N = 4$.

$$\frac{\mathrm{d}^2E(N)}{\mathrm{d}N^2} = B, \quad N \neq 4 \tag{10}$$

Equation 10 is illustrated in Figure 1c with a purple dashed line, where a reasonable fit to the data (aside from a deviation at a charge of 4+) is observed. The discrepancy at 4+ is indicative of the jump discontinuity, Figure 1b.

We next turn our attention to the nature of the electronic structure of the AgNC. In Figure 2a−d we show the spin resolved band gap of the AgNC modeled as a function of the

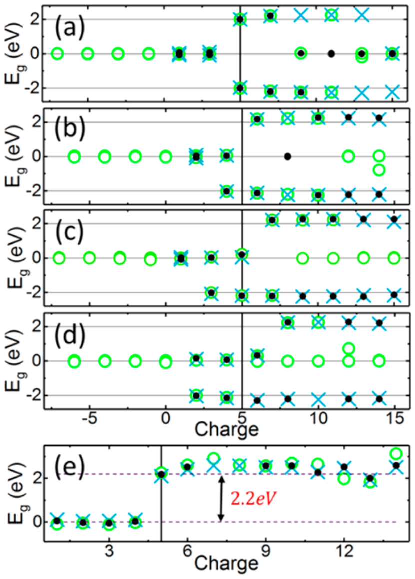

Figure 2. Spin resolved band gap as a function of charge for the (a) singlet, (b) doublet, (c) triplet, and (d) quartet ground-state configuration. Note that the band gap for beta electrons is multiplied by −1 for clarity. (e) To compare classical results with first-principles calculations, we replot Figure 1b with the linear background removed $\left(\frac{\mathrm{d}E}{\mathrm{d}N} = A_1 + BN\right)$. The jump discontinuity here is very similar in magnitude to the first-principles calculation of the band gap. Note that, for each first-principles calculation, PBE, HSE06, and B3LYP functionals were used, where the same key used to differentiate the functionals in Figure 1 is used here: circle, cross, and dot stand for PBE, HSE06, and B3LYP data, respectively.

total number of electrons, per eq 2a. Note that due to the spin resolved nature of these calculations, we determine a band gap for both alpha, $\Delta\varepsilon_{\alpha}^{\mathrm{gap}}(N, \Delta N_{\uparrow\downarrow})$, and beta, $\Delta\varepsilon_{\beta}^{\mathrm{gap}}(N, \Delta N_{\uparrow\downarrow})$, electrons. To visually display both, the band gap value of the beta electrons is multiplied by −1 in Figure 2a−d. Examination of the band gap is one the most efficient means to determine whether a material is an insulator (>3 eV), semiconductor (~1 to 3 eV), or conductor (≪1 eV). In this case, we are most interested in a semiconducting band gap (~1 to 3 eV), as this has the highest potential for fluorescence. In Figure 2a−d we see that that the band gap is semiconducting (~2 eV) in nature at a charge of 5+ or greater regardless of GS configuration. Once the band gap is opened, the gap value remains independent of charge and exchange correlation functional. We take a quick aside to mention that several experimental reports have emphasized the influence of charge on the overall PL. Interestingly, our calculations indicate that, although a high charge is necessary for PL, it has a negligible impact on the HOMO−LUMO gap once it is opened, indicating that factors such as morphology and passivation play a more pivotal role in determining the observed PL.

Reminiscent of the discontinuity in $\frac{\mathrm{d}E_{\mathrm{tot}}(N)}{\mathrm{d}N}$, shown in Figure 1b at a charge of 5+, we see that the band gap for both alpha and beta electrons is open only when the charge is 5+ or greater, regardless of GS configuration. To further exemplify the resemblance between the discontinuity in $\frac{\mathrm{d}E_{\mathrm{tot}}(N)}{\mathrm{d}N}$ and the calculated band gap, in Figure 2e we replot $\frac{\mathrm{d}E_{\mathrm{tot}}(N)}{\mathrm{d}N}$ with a subtracted background of $BN + A_1$. This results in two lines with no slope per eq 11 below.

$$\frac{\mathrm{d}E(N)}{\mathrm{d}N} = \begin{cases} 0, & N < 5 \\ \Delta A, & N > 5 \end{cases} \tag{11}$$

With the slope of the line removed one can see that not only does the discontinuity occur at the same charge but also has a comparable amplitude to the DFT calculated band gap.

In Figure 3c,d, we show the DOS for the charged and uncharged AgNC, respectively. The overall structure of the DOS for both models is very similar, but the extra electrons in the neutrally charged cluster are located in what would be the conduction band of the charged model, creating a "pseudogap" and limiting any potential for optical emission. Here "pseudogap" refers to a subgap of 0.5 eV or greater in the valence band of the DOS.

The neutral cluster has a zero HO-LU gap, as can be seen in Figure 3d. However, there are two noticeable pseudogaps, one between $\mathrm{HO}_{\alpha} - 3$ and $\mathrm{HO}_{\alpha} - 2$ and the other between $\mathrm{HO}_{\beta} - 2$ and $\mathrm{HO}_{\beta} - 1$. The DOS of the neutral model looks similar to a DOS of an n-doped semiconductor; however, the model with a + 5 charge exhibits an open gap, as shown in Figure 3c. The response of the electronic structure to the change in charge is schematically summarized in Figure 3a. We show the spin resolved band gap for alpha and beta electrons with N equal to 5+, 7+, 9+, and 11+ with open gaps in the singlet GS configuration, $\Delta N_{\uparrow\downarrow} = 0$. As just mentioned, the magnitude of these gaps appears to be independent of the total charge, yet as electrons are removed and the charge increases and the Fermi energy drops.

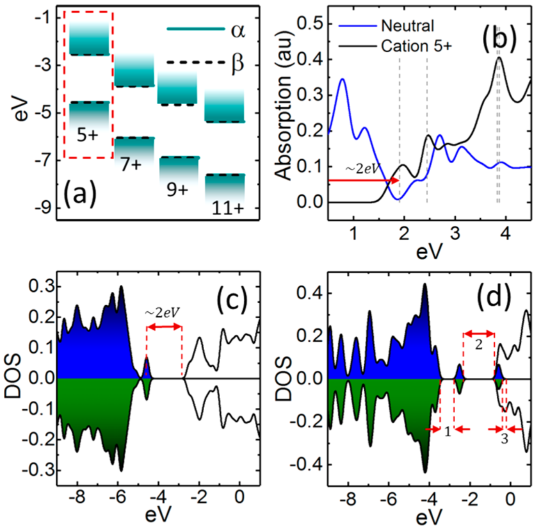

Figure 3. (a) Spin resolved band gaps for the singlet ground state configuration for charges of 5+, 7+, 9+, and 11+. (b) The absorption spectra for a silver nanocluster in the 5+ charge state and neutral state are compared with the spin resolved density of states for the (c) charged and (d) neutral state, for reference. Note that in (c) and (d) the DOS for beta electronic states are multiplied by −1 and the shaded and unshaded regions represent occupied and unoccupied KS-orbitals, respectively. The vertical dashed lines in (b) are the four most probable optical transitions. In (d) labels 1 and 2 represent the pseudogaps while label 3 represents the formal gap, which is nearly zero in this case. Opening the gap by going from the neutral to 5+ charge can be interpreted as the removal of 5 electrons from the 5 degenerate orbitals at the bottom of the conduction band in the neutral AgNC. Note that there were no constraints on spin multiplicity, providing singlet and doublet for (c) and (d) as energy minima.

In Figure 3b, we calculate the absorption spectra according to eqs 3a, 3b, and 4 for the AgNC in the singlet 5+ and doublet neutral configuration. The neutrally charged AgNC exhibits broad absorption from 0 to 4 eV, again, similar to the intraband transitions in an n-doped semiconductor.[80] However, due to the open gap nature of the charged AgNC, there are no transitions in the IR range. We also show the four most probable transitions in the absorption spectra of the charged AgNC, denoted by vertical dashed lines. Expanding upon this, Table 1 includes the ten most probable elementary excitations across the band gap. The elementary excitations are labeled by the pair of orbitals (HO − i and LU + j) involved in the transition, their corresponding oscillator strength, $f_{\mathrm{HO}-i,\mathrm{LU}+j}$, and the thermalization rates, which will be introduced later. Interestingly, most of the bright transitions occur from the top of the valence band to a relatively large number of orbitals away from the bottom of the conduction band. Typical orbitals involved in absorption and emission are shown in Figure S3 where orbitals reside in the core prior to excitation and then are promoted to orbitals primarily located on the ligand and moderately hybridized with the core region of the cluster. Recombination via Kasha's rule would then occur in the AgNC where both the HOMO and LUMO reside on the core.

Using TDDFT methodologies (as opposed to the DFT/IOA methodologies employed here), Bae et al. calculated the absorption spectra of bare AgNCs possessing the same icosahedral shape and charge as the AgNCs modeled here. The TDDFT calculations resulted in absorption spectra that are blue-shifted compared to the DFT/IOA values.[36] Although it has been shown that absorption spectra calculated using TDDFT are linearly shifted in energy in comparison to DFT spectra,[55,81,82] we suspect that the difference in passivation is

DOI: 10.1021/acs.jpcc.7b04870
J. Phys. Chem. C 2017, 121, 23875−23885

Table 1. Representative[a] Inter-band Excitations under the Independent Orbital Approximation Represented by Pairs of Occupied (Hole) and Unoccupied (Electron) Orbitals[b]

initial orbital, i	final orbital, j	oscillator strength, f_{ij}	energy of transition (eV)	thermalization lifetimes (τ_e/τ_h) (ps)	thermalizations rates (k_e/k_h) (ps^{-1})
HO − 2 (319)	LU + 5 (327)	3.593789	2.4744	0.3111/3.3146	3.2138/0.3017
HO − 1 (320)	LU + 25 (347)	3.125815	3.8477	0.9161/5.3967	1.0915/0.1853
HO − 1 (320)	LU + 23 (345)	1.634268	3.7894	0.9916/5.3967	1.0084/0.1853
HO (321)	LU + 26 (348)	1.550391	2.6759	0.9091/−	1.1000/−
HO − 2 (319)	LU + 10 (332)	1.55031017	2.6759	0.4639/3.3146	2.1558/0.3017
HO (321)	LU + 2 (324)	1.38873756	2.22	0.1841/−	5.4315/−
HO − 2 (319)	LU + 8 (330)	1.28777306	2.6204	0.3463/3.3146	2.8875/0.3017
HO − 1 (320)	LU + 35 (357)	1.27029564	4.3379	0.9322/5.3967	1.0727/0.1853
HO − 2 (319)	LU (322)	1.2570283	2.0617	−/3.3146	−/0.3017
HO − 2 (319)	LU + 1 (323)	1.21181109	2.1431	0.0540/3.3146	18.5215/0.3017
HO (321)	LU (322)	0.260736	2.0137		

[a] This was all calculated at the PBE level of theory. [b] Shown excitations are chosen out of about 18 000 elementary excitations based on larger values of the oscillator strength and the transition energies vicinity to the bandgap. Note that oscillator strength values computed by eq 3a are not normalized here. The last two columns represent thermalization rates and lifetimes for electrons and holes for each given excitation, computed by fitting the data of eqs S2−S5 to a single exponential decay function. Interestingly, most of the bright transitions occur from the top of the valence band to relatively large number of orbitals away from the bottom of the conduction band.

Table 2

source	no. of Ag atoms	charge	gap (eV) PBE/B3LYP/HSE06
theory (this work)	13	+5	2.0137/2.0050/2.0047[a]
experimental (Petty, ref 28)	10	+6	[b]

[a] Because the +5 model was in the singlet configuration the band gap for alpha and beta electrons were the same. [b] Petty et al. did not specifically list an emission spectra.

more likely the root cause of the observed discrepancy. Furthermore, Bae et al. also calculated a corresponding band gap for an icosahedral AgNC with charges of −5, −1, and +5 to be 0.32, 0.05, and 2.93 eV, respectively, where the authors correlated the larger band gaps in the −5 and +5 charge states as "magic number" superatom clusters, as discussed in greater detail in section 4.

Modeling electronic dynamics and computing photoemission is numerically costly. Consequently, after identification of the most promising configurations, we then focus our attention on one representative example, the 5+ singlet state. As a prerequisite to calculating PL, a molecular dynamics (MD) simulation was conducted on the AgNC in the 5+ singlet GS configuration. Here the total energy of the system was found to randomly fluctuate near approximately $E_{\text{tot}}(t) = -1052 \pm 0.5$ eV, as shown in Figure 4a. When measuring the distance between the center silver atom (Ag_c) and the other 12 surface silver atoms of our model, we found that the Ag_c−Ag distance harmonically oscillates by ~0.1 Å with a mean distance of 2.8 Å. These higher amplitude oscillations arise from all normal modes, not only the Ag−N stretch. The distance of the three nitrogen atoms in cytosine from the core silver atom (Ag_c−N) fluctuates near 5, 6, and 7 Å, on average. One could imagine that the jittery oscillations of nitrogen atoms are expected due to the relatively low molecular weight of N compared to Ag and the restricted degrees of freedom due to the ring structure of cytosine. Furthermore, the greatest oscillations are found for the primary nitrogen, whereas the amplitude of oscillation of the secondary nitrogen atoms are damped, again likely due to reduced degrees of freedom.

As detailed in the Methodology section, the fluctuation of the energy of the KS orbitals along the MD trajectory, $\varepsilon_\sigma^i(t)$, can be determined as displayed in Figure 4d,e. The details related to nonadiabatic couplings, their autocorrelation functions, and the relevant values of the Redfield Tensor elements are shown in Figure S4 of the SI. The time dependent KS orbitals with nonadiabatic coupling (NAC) in conjunction with the Redfield master equation can be used to find orbital occupation as a function of time for any initial excitation specified by the active pairs of orbitals, HO − i and LU + j.[51]

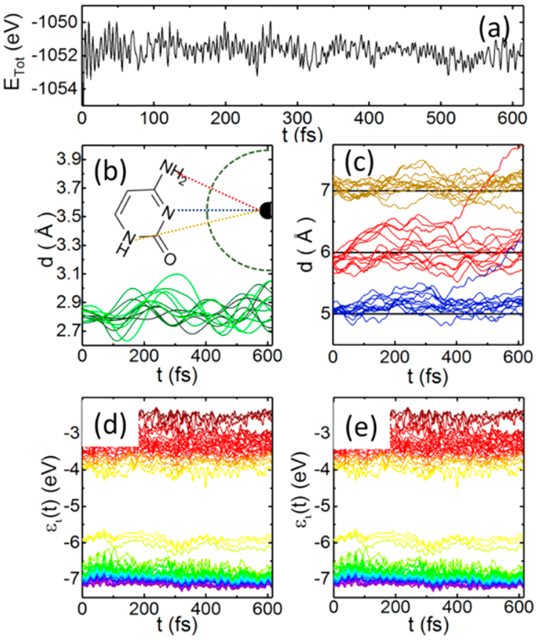

Figure 4. Room temperature molecular dynamics simulations were conducted for the silver nanocluster with a 5+ singlet ground state configuration. The (a) total energy as well as the distance of (b) outer silver atoms and the (c) nitrogen atoms in cytosine to the center silver atom were determined. The colors in (b) and (c) are coded to match the inset of (b). From the molecular simulations, spin-resolved time dependent Kohn−Sham orbitals were determined for (d) alpha and (e) beta electrons with the PBE functional.

For most excitations, there are two typical trends: (i) the relaxation of one carrier, electron or hole, is independent of where the second carrier is excited to and (ii) the relaxation occurs in a cascade fashion

DOI: 10.1021/acs.jpcc.7b04870
J. Phys. Chem. C 2017, 121, 23875−23885

$$\mathrm{LU} + j \rightarrow \mathrm{LU} + (j-1) \rightarrow \ldots \rightarrow \mathrm{LU} + 2 \rightarrow \mathrm{LU} + 1 \rightarrow \mathrm{LU}$$

$$\mathrm{HO} - i \rightarrow \mathrm{HO} - (i-1) \rightarrow \ldots \rightarrow \mathrm{HO} - 2 \rightarrow \mathrm{HO} - 1 \rightarrow \mathrm{HO}$$

Based on these trends we deduce that the final stages of the cascade, which are the most important for photoemission, occur through the same sequence of orbitals with the same rates, for a broad range of excitations. A representative example of this thermalization process for an initial excitation of LU + 25 and HO − 25 is illustrated in Figure 5a,b, respectively, which depict an electron relaxing to the LUMO within 300 fs and a hole thermalizing to HO − 2 in ~250 fs and then subsequently relaxing to the HOMO by ~500 fs. The resulting HOMO−LUMO excitation then waits to radiatively recombine via Kasha's rule.[56]

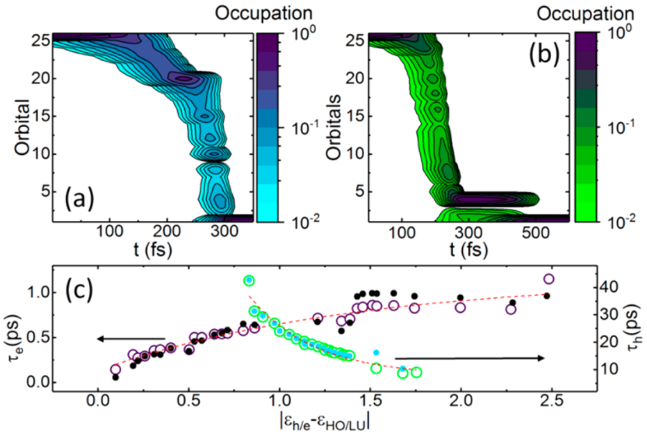

Figure 5. Orbital occupation for alpha (a) electrons and (b) holes as a function of time calculated for the silver nanocluster in the 5+ singlet ground state configuration, thermalizing from LUMO+25 to the LUMO and from HOMO+25 to the HOMO, respectively. (c) Calculated electron and hole thermalization lifetimes as a function of the energy difference between the corresponding band edge and initial excitation level. The solid and open circles represent alpha and beta electrons, respectively, while the black and purple symbols are electron lifetimes and the green and blue symbols represent hole lifetimes. The alpha and beta electrons of both the hole and electron lifetimes are fit with an exponential function (red dashed curve).

Computed results for the time dependent occupation of orbitals can be used to find observables: (i) the time dependent charge distribution (Figure S5 in the SI) and (ii) the expectation values of the energy of a KS carrier, $\langle E^{e}\rangle(t)$ and $\langle E^{h}\rangle(t)$ according to eqs S2−S5 of the SI. The change in average energy of an electron, $\langle E^{e}\rangle(t)$, and hole, $\langle E^{h}\rangle(t)$, as they thermalize to the band edge are illustrated in another example of excited state dynamics shown in Figure S6(a) and (d) of the SI. This explicit example is computed for the initial conditions corresponding to an excitation from HO − 10 to LU + 10.

Next, we explore the response of the excited state dynamics to changes in the initial conditions or initial excitation. The initial excitation of a charge carrier can be labeled in two fashions: first, by orbital index and second, by an offset of orbital energy from the band edge; $|\varepsilon_i - \varepsilon_{\mathrm{LU}}|$ for electrons and $|\varepsilon_{\mathrm{HO}} - \varepsilon_i|$ for holes. Here, the dependence on initial excitation is best visualized as a relaxation time, $\tau = k^{-1}$, versus initial excitation energy. The relaxation time of both alpha and beta electrons, $\tau_e = (k_e)^{-1}$ in Table 1 and Figure 5c, are in accordance with the band gap law such that the lifetime increases with increasing excitation energy.[83] Contrary to this, however, the hole relaxation times, $\tau_h = (k_h)^{-1}$, have the opposite trend, where it is possible that this is due to the dense spacing of the KS orbital energy in the valence band.

Methods outlined in eq 8a were used to calculate the spin resolved PL, where Figure S6(c) and (f) shows the results. A strong peak centered at approximately 2 eV dwarfs smaller peaks in the low energy infrared region of the spectrum associated with nonradiative recombination pathways. The summation of spin resolved PL by eq 8b was used to create the overall PL spectrum in Figure 6, where the strong peak is centered at approximately 610 nm. Also in Figure 6 we plot the absorption spectra according to eq 4 as well as experimentally observed PL and absorption data from ref 19 for oligonucleotide capped AgNCs with a 540 nm excitation.

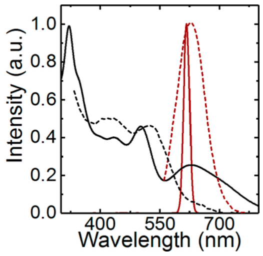

Figure 6. Normalized calculated PL (solid red line) and absorption (solid black line) spectra for the 5+ singlet model with experimental PL (dashed red line) and absorption spectra (dashed black line) from Petty (ref 22).

4. DISCUSSION AND INTERPRETATION

The current state of the data reveals two main points that need to be discussed in greater detail; (a) the presence and interpretation of the discontinuity in $\frac{\mathrm{d}E_{\mathrm{tot}}}{\mathrm{d}N}$ and (b) the validity of an open-gap configuration for charges of 5+ and its implications for a high-charge state as a requirement for PL in AgNCs. We begin this discussion with the former, the presence of the discontinuity.

4.1. Jump Discontinuity in $\frac{\mathrm{d}E_{\mathrm{tot}}(N)}{\mathrm{d}N}$.

We rationalize the presence of the discontinuity in $\frac{\mathrm{d}E_{\mathrm{tot}}}{\mathrm{d}N}$ using an electrostatic approach for a metal sphere. First, the energy required to remove N electrons from a neutral metal sphere $E_{\mathrm{ion}}(N)$ can be modeled according to Coulomb's Law as given by eq 12 below

$$E_{\mathrm{ion}}(N) = \Delta E_{\mathrm{tot}} = E_{\mathrm{tot}}(N) - E_{\mathrm{tot}}(0) = -\frac{1}{\varepsilon_R}\frac{(Ne)(-Ne)}{|R_0|} \tag{12}$$

Here R_0 is the radius of the conducting metal sphere and ε_R is the dielectric constant of the surrounding material in atomic units. The energy dependence scales as the second power of the number of electrons, N, and the first derivative of this ionization term leads to $\frac{\mathrm{d}E_{\mathrm{ion}}}{\mathrm{d}N} = \frac{2e^2}{\varepsilon|R_0|}N$. Fitting the DFT derived data in Figure 1b, we find a very similar trend with $\frac{\mathrm{d}E_{\mathrm{ion}}}{\mathrm{d}N} = A_{1,2} + BN$, where $A_{1,2}$ is a constant for the data on either side of the jump discontinuity at 5+. We expect this constant to be directly related to the quantum nature of the

DOS, which is neglected in the classical approach taken here. Gaps in the DOS will increase the energy required to remove the electron. It is probable that this is the root cause for both of the observed deviations between eq 12 and the actual fit of the data in eq 9. The most prominent difference between eqs 9 and 12 lies in the presence of the constant $A_{1,2}$, which we again assume reflects the difference between the classical model and the quantum nature of the system. With the sudden jump at a charge of 5+, we assume that this must have a strong correlation to the presence of the bandgap, due in part to the resemblance of ΔA to the DFT calculated band gap. We further assume that the band gap can be approximated from the energy of ionization, E_{ion}, i.e., removal of one electron using eq 13 below

$$\mathrm{d}E_{\text{ion}} \approx E^{\text{gap}}(N, R_0, \varepsilon) = -\frac{2}{\varepsilon}\frac{(Ne)(-e)}{|R_0|} = BN \tag{13}$$

From this we see that the band gap of the nanocluster is a function of the charge and size of the nanocluster as well as the dielectric constant of the surrounding medium.

However, from the DFT generated results we see that the band gap is weakly coupled to the charge aside from the clear dependence at a charge of 5+ in Figure 2a−d. Now, we did not explicitly study how variations in the surrounding media would affect the PL, but this has been examined in the literature, with several groups showing that the stabilizing ligand and the dispersing solvent play a critical role in the observed PL.[21,25−27] For instance, Richards et al. and Copp et al. were able to tune the AgNC's PL by changing the DNA sequences passivating the AgNC surface,[20,21] while Diez et al. demonstrated strong coupling between the solvent and AgNC PL.[26]

Both systems can be explained using the simple model detailed in eq 13. The calculated data from Figure 1b have a slope of $B \approx 0.439$. Using this in eq 13, we get $E^{\text{gap}}(+5, 2.756\ \text{Å}, \varepsilon) = 0.439{*}5 = 2.195$ eV. By solving eq 13 for the only variable left (i.e., the dielectric constant), we obtain a value of 12.1. To the best of our knowledge, the dielectric constant of cytosine is not given explicitly, but with the volume and polarizability one can use the Clausius−Mossotti relation[84] to determine a dielectric constant, which ends up being approximately 3.83 in this case. More details on this calculation can be found in the SI.

Because these nanoparticles are dispersed in water, which has a substantially larger dielectric constant of 80.1, we would expect this to play a role in the overall dielectric constant of the medium surrounding the nanoparticle. Here we employ a simple rule of mixtures, $\varepsilon_{\text{mix}} = \phi_{\text{cyt}}\varepsilon_{\text{cyt}} + \phi_{\text{water}}\varepsilon_{\text{cyt}}$, where ϕ is the volume fraction. One can solve for ϕ_{cyt} and ϕ_{water} knowing that $1 = \phi_{\text{cyt}} + \phi_{\text{water}}$, which leads to $\phi_{\text{cyt}} = 0.89$ and $\phi_{\text{water}} = 0.11$. We find this solution to be reasonable due to the fact that cytosine is in direct contact with the silver sphere. As a result, its dielectric constant would have the largest impact on the total dielectric constant, while in contrast very few water molecules can approach the nanocluster and affect it.

Another way to examine the jump discontinuity at 5+ is through the lens of superatom chemistry. As mentioned in the Introduction, the first of the four main directions in the computational modeling of noble metal clusters entails a determination of the morphology of that cluster and whether that cluster is purely metallic or an organo-metallic complex. Although explicit examination of the specific shape and morphology of the cluster is outside the scope of this work, we will briefly discuss the implications here. Small clusters of metallic atoms, or "superatoms", can take on significantly different properties from the bulk. The early work by Knight showed that in a cool gas of sodium atoms, the atoms would condense into clusters containing a specific number of atoms; 8, 20, 40, etc.,[85,86] where the specific number of atoms in a cluster was attributed to electronic shell closure.

Similar to the noble gases with their filled shells, superatoms can also exhibit exceptional stability with a valence electron count of $n^* = 2, 8, 18, 34, 58, 92, 138, \ldots$ again due to shell closure.[30] Directly relevant to the work here, Häkkinen and coworkers derived a simple arithmetic expression to predict whether a superatom with organic ligands has shell closure; $n^* = N\nu_{\text{A}} - M - z$, where n^* is the valence electron count corresponding to the list above, N is the number of metallic atoms, ν_{A} is the number of valence electrons in the metallic atom, and M is the number of electron withdrawing ligands, assuming each ligand withdraws one electron and z is the overall charge.

In the AgNC studied here, a shell closure would correspond to a charge, z, of 5− and 5+ with a shell closure, n^*, of 18 and 8, respectively, due to the 13 metal atoms and the $5s^1$ valence electron in each atom [e.g., $8 = (13)(1) - 0 - 5$ and $18 = (13)(1) - 0 + 5$]. This indicates that the ligand or DNA does not withdraw electrons from the AgNC core and perhaps a more complex ligand structure is adopted. Alternatively, if one explicitly counts the 10 electrons in the d orbitals of silver based on the Aufbau principle, $\text{Ag}^{(0)} = [\text{Kr}]4\text{d}^{10}5\text{s}^1$, a shell closure is still observed at a charge of 5+ with a magic shell closure of 138 electrons [e.g., $138 = (13)(11) - 0 - 5$].

Ligand stabilization of gold nanoclusters was found to occur through a metal−ligand adduct; $\text{M}^{(+)}$-Ligand with a pure neutral gold core.[30] This type of complex could also be occurring in DNA complexed AgNCs, where there is an inner neutral core of silver atoms surrounded by positively charged Ag^+-DNA adducts. In fact, the same type of complex has already been hypothesized by Petty et al.[28] and Copp et al.[20] in their work on DNA-AgNC complexes.

4.2. Model Validity.

This brings us to the final part of our discussion: can we trust the DFT generated results and if so, what are the implications? In Figure 2 we showed the DFT generated band gap of the AgNC. The band gap was not present in AgNC with a charge lower than 5+, but once a high charge state was achieved the gap opened to approximately 2 eV with a weak coupling to the total charge. With these calculations, we are aware of and concerned about the possibility of self-interaction errors. Self-interaction errors are rooted in the exchange correlation functionals used in any DFT calculation and have been an area of growing academic interest. The error arises due to the functionals inability to remove an electron's interaction with itself. This causes erroneous calculations of different values such as the total energy. Because of this, we used three different functionals to perform each calculation; one GGA functional (PBE) and two hybrid functionals (HSE06 and B3LYP). The GGA functional is particularly susceptible to this error, yet hybrid functions such as HSE06 can limit the effects of self-interaction errors and have been moderately successful in predicting the band gap of nanoscale semiconductors.[87,88] From our calculations, we found that all three functionals show excellent agreement in predicting the magnitude of the band gap for each charge.

TDDFT approaches are particularly good for limiting self-interaction errors. Herein we find the band gap of the 5− and

5+ AgNC with electronic shell closures of 8 and 18 to be 0.02 and 2.01 eV, respectively, while TDDFT calculations of a bare icosahedral AgNC in the 5− and 5+ state approximate the band gap as 0.32 and 2.93 eV, respectfully.[36] Although the explicit magnitude of the gap for these models differs from what is calculated here, we expect the primary difference in ligand passivation (cytosine vs bare) to have a larger impact than the choice of computational method.

5. CONCLUSIONS

Silver nanoclusters are ideal fluorophores for biological systems with their high photostability, relatively nontoxic nature, and small footprint.[1] Yet, despite several inspiring proof-of-concept sensors[25,28,29] and biolabels,[24] a compelling model of the PL has been lacking. Herein, spin-resolved constrained DFT calculations of an icosahedron shaped AgNC passivated with cytosine is presented.

Due to the sensitivity of the optical properties of the nanoparticles to their surrounding environment, the electronic structure of the AgNC was calculated for various charges, where it was found that a relatively high charge of 5+ or greater is necessary for the nanocluster to become optically active for electrons of either spin, although charge otherwise played little role in the overall PL. Although such a high charge raises concerns about a self-interaction errors, the consistency of calculations performed with hybrid functionals (HSE06 and B3LYP) and a standard GGA functional (PBE), as well as the similarities with TDDFT calculations[36] and several experimental works,[19,20,28] and superatom closed valence shell concept,[30] lends further confidence to the reported results.[28]

Furthermore, we report a new method to estimate the band gap of semiconducting nanoparticles through careful examination of the total energy as a function of charge using a classical electrostatics method. The first derivative with respect to charge of the total energy was found to be linear in nature, yet a discontinuity was present at a charge of 5+, where the amplitude of the jump coincided with the calculated band gap of approximately 2 eV. Using a classic Coulombic model, we rationalized the observed behavior. We proposed that the band gap is inversely dependent to the dielectric constant of the surrounding material, which intuitively speaks to the nature of the sensitivity of photoemission to surface passivation.

The methodologies presented for the calculation of spin resolved PL are general and can be applied to a broad variety of other nanoscale systems. Such application is exemplified by a model silver nanocluster for proof of concept, thus overcoming a lack of atomistic simulations for the PL properties in such systems. The calculated PL and absorption spectra show similarities to experimental data, giving credence to the validity of the methodologies described here. In this report, the size, morphology, and surface passivation effects are not explicitly explored. In nanoscale systems, these variables are expected to impact a variety of photophysical phenomena and are targets of future study.

■ ASSOCIATED CONTENT

Ⓢ Supporting Information

The Supporting Information is available free of charge on the ACS Publications website at DOI: 10.1021/acs.jpcc.7b04870.

Additional information on electronic structure calculations and electron dynamics (PDF)

Animation of 300K ab initio molecular dynamics trajectory of cytosine-protected Ag_{13} icosahedral nanocluster (MPG)

■ AUTHOR INFORMATION

Corresponding Author

*E-mail: Dmitri.Kilin@ndsu.edu.

ORCID

Erik K. Hobbie: 0000-0001-6158-8977
Sergei Tretiak: 0000-0001-5547-3647
Dmitri S. Kilin: 0000-0001-7847-5549

Notes

The authors declare no competing financial interest.

■ ACKNOWLEDGMENTS

The authors thank Doug Jennewein for maintaining the USD high performance computing cluster. Authors thank Jen Martinez (CINT, LANL) and Svetlana Kilina (NDSU) for inspiring discussions and sharing ideas. The authors would also like to thank the members of the Kilin and Kilina group Jon Vogel, Yulun Han, Aaron Forde, Dane Hogoboom, Levi Lystrom, Mohammed Jabed, and Brendan Gifford for fruitful discussion and suggestions. D.K. acknowledges support of NSF award CHE-1413614 for methods development and by DOE, BES Chemical Sciences, NERSC Contract No. DE-AC02−05CH11231, allocation Award 91202, "Computational Modeling of Photocatalysis and Photoinduced Charge Transfer Dynamics on Surfaces". This work was performed in part at the Center for Integrated Nanotechnologies (CINT), a U.S. Department of Energy, and the Office of Basic Energy Sciences user facility, at Los Alamos National Laboratory (LANL).

■ REFERENCES

(1) Diez, I.; Ras, R. H. A. Fluorescent Silver Nanoclusters. *Nanoscale* **2011**, *3*, 1963−1970.

(2) Stohs, S. J.; Bagchi, D. Oxidative Mechanisms in the Toxicity of Metal-Ions. *Free Radical Biol. Med.* **1995**, *18*, 321−336.

(3) Derfus, A. M.; Chan, W. C. W.; Bhatia, S. N. Probing the Cytotoxicity of Semiconductor Quantum Dots. *Nano Lett.* **2004**, *4*, 11−18.

(4) Valko, M.; Morris, H.; Cronin, M. T. D. Metals, Toxicity and Oxidative Stress. *Curr. Med. Chem.* **2005**, *12*, 1161−1208.

(5) Gidlow, D. A. Lead Toxicity. *Occupational Medicine-Oxford* **2004**, *54*, 76−81.

(6) Papanikolaou, N. C.; Hatzidaki, E. G.; Belivanis, S.; Tzanakakis, G. N.; Tsatsakis, A. M. Lead Toxicity Update. A Brief Review. *Med. Sci. Monit.* **2005**, *11*, RA329−RA336.

(7) Elbaradei, A.; Brown, S. L.; Miller, J. B.; May, S.; Hobbie, E. K. Interaction of Polymer-Coated Silicon Nanocrystals with Lipid Bilayers and Surfactant Interfaces. *Phys. Rev. E: Stat. Phys., Plasmas, Fluids, Relat. Interdiscip. Top.* **2016**, *94*, 9.

(8) Delehanty, J. B.; Mattoussi, H.; Medintz, I. L. Delivering Quantum Dots into Cells: Strategies, Progress and Remaining Issues. *Anal. Bioanal. Chem.* **2009**, *393*, 1091−1105.

(9) Buzea, C.; Pacheco, II; Robbie, K. Nanomaterials and Nanoparticles: Sources and Toxicity. *Biointerphases* **2007**, *2*, MR17−MR71.

(10) Jiang, W.; Kim, B. Y. S.; Rutka, J. T.; Chan, W. C. W. Nanoparticle-Mediated Cellular Response Is Size-Dependent. *Nat. Nanotechnol.* **2008**, *3*, 145−150.

(11) Braydich-Stolle, L.; Hussain, S.; Schlager, J. J.; Hofmann, M. C. In Vitro Cytotoxicity of Nanoparticles in Mammalian Germline Stem Cells. *Toxicol. Sci.* **2005**, *88*, 412−419.

(12) Colvin, V. L. The Potential Environmental Impact of Engineered Nanomaterials. *Nat. Biotechnol.* **2003**, *21*, 1166−1170.

(13) Wang, X. Z.; Yang, Y.; Li, R. F.; McGuinnes, C.; Adamson, J.; Megson, I. L.; Donaldson, K. Principal Component and Causal Analysis of Structural and Acute in Vitro Toxicity Data for Nanoparticles. *Nanotoxicology* **2014**, *8*, 465−476.

(14) King-Heiden, T. C.; Wiecinski, P. N.; Mangham, A. N.; Metz, K. M.; Nesbit, D.; Pedersen, J. A.; Hamers, R. J.; Heideman, W.; Peterson, R. E. Quantum Dot Nanotoxicity Assessment Using the Zebrafish Embryo. *Environ. Sci. Technol.* **2009**, *43*, 1605−1611.

(15) Meng, H.; Chen, Z.; Xing, G.; Yuan, H.; Chen, C.; Zhao, F.; Zhang, C.; Zhao, Y. Ultrahigh Reactivity Provokes Nanotoxicity: Explanation of Oral Toxicity of Nano-Copper Particles. *Toxicol. Lett.* **2007**, *175*, 102−110.

(16) Wiecinski, P. N.; Metz, K. M.; Heiden, T. C. K.; Louis, K. M.; Mangham, A. N.; Hamers, R. J.; Heideman, W.; Peterson, R. E.; Pedersen, J. A. Toxicity of Oxidatively Degraded Quantum Dots to Developing Zebrafish (Danio Rerio). *Environ. Sci. Technol.* **2013**, *47*, 9132−9139.

(17) Yu, J.; Patel, S. A.; Dickson, R. M. In Vitro and Intracellular Production of Peptide-Encapsulated Fluorescent Silver Nanoclusters. *Angew. Chem., Int. Ed.* **2007**, *46*, 2028−2030.

(18) Schultz, D.; Gardner, K.; Oemrawsingh, S. S. R.; Markesevic, N.; Olsson, K.; Debord, M.; Bouwmeester, D.; Gwinn, E. Evidence for Rod-Shaped DNA-Stabilized Silver Nanocluster Emitters. *Adv. Mater.* **2013**, *25*, 2797−2803.

(19) Petty, J. T.; Zheng, J.; Hud, N. V.; Dickson, R. M. DNA-Templated Ag Nanocluster Formation. *J. Am. Chem. Soc.* **2004**, *126*, 5207−5212.

(20) Copp, S. M.; Schultz, D.; Swasey, S.; Pavlovich, J.; Debord, M.; Chiu, A.; Olsson, K.; Gwinn, E. Magic Numbers in DNA-Stabilized Fluorescent Silver Clusters Lead to Magic Colors. *J. Phys. Chem. Lett.* **2014**, *5*, 959−963.

(21) Richards, C. I.; Choi, S.; Hsiang, J. C.; Antoku, Y.; Vosch, T.; Bongiorno, A.; Tzeng, Y. L.; Dickson, R. M. Oligonucleotide-Stabilized Ag Nanocluster Fluorophores. *J. Am. Chem. Soc.* **2008**, *130*, 5038−5039.

(22) Koszinowski, K.; Ballweg, K. A Highly Charged Ag-$_6^{4+}$ Core in a DNA-Encapsulated Silver Nanocluster. *Chem. - Eur. J.* **2010**, *16*, 3285−3290.

(23) Crooks, R. M.; Lemon, B. I.; Sun, L.; Yeung, L. K.; Zhao, M. Q. Dendrimer-Encapsulated Metals and Semiconductors: Synthesis, Characterization, and Applications. *Top. Curr. Chem.* **2001**, *212*, 81−135.

(24) Yu, J. H.; Choi, S. M.; Richards, C. I.; Antoku, Y.; Dickson, R. M. Live Cell Surface Labeling with Fluorescent Ag Nanocluster Conjugates. *Photochem. Photobiol.* **2008**, *84*, 1435−1439.

(25) Yeh, H. C.; Sharma, J.; Han, J. J.; Martinez, J. S.; Werner, J. H. A DNA-Silver Nanocluster Probe That Fluoresces Upon Hybridization. *Nano Lett.* **2010**, *10*, 3106−3110.

(26) Diez, I.; Pusa, M.; Kulmala, S.; Jiang, H.; Walther, A.; Goldmann, A. S.; Muller, A. H. E.; Ikkala, O.; Ras, R. H. A. Color Tunability and Electrochemiluminescence of Silver Nanoclusters. *Angew. Chem., Int. Ed.* **2009**, *48*, 2122−2125.

(27) Diez, I.; Jiang, H.; Ras, R. H. A. Enhanced Emission of Silver Nanoclusters through Quantitative Phase Transfer. *ChemPhysChem* **2010**, *11*, 3100−3104.

(28) Petty, J. T.; Sergev, O. O.; Ganguly, M.; Rankine, I. J.; Chevrier, D. M.; Zhang, P. A Segregated, Partially Oxidized, and Compact Ag-10 Cluster within an Encapsulating DNA Host. *J. Am. Chem. Soc.* **2016**, *138*, 3469−3477.

(29) Petty, J. T.; Sergev, O. O.; Kantor, A. G.; Rankine, I. J.; Ganguly, M.; David, F. D.; Wheeler, S. K.; Wheeler, J. F. Ten-Atom Silver Cluster Signaling and Tempering DNA Hybridization. *Anal. Chem.* **2015**, *87*, 5302−5309.

(30) Walter, M.; Akola, J.; Lopez-Acevedo, O.; Jadzinsky, P. D.; Calero, G.; Ackerson, C. J.; Whetten, R. L.; Gronbeck, H.; Hakkinen, H. A Unified View of Ligand-Protected Gold Clusters as Superatom Complexes. *Proc. Natl. Acad. Sci. U. S. A.* **2008**, *105*, 9157−9162.

(31) Harb, M.; Rabilloud, F.; Simon, D.; Rydlo, A.; Lecoultre, S.; Conus, F.; Rodrigues, V.; Félix, C. Optical Absorption of Small Silver Clusters: Ag$_n$, (n = 4−22). *J. Chem. Phys.* **2008**, *129*, 194108.

(32) Ramazanov, R. R.; Sych, T. S.; Reveguk, Z. V.; Maksimov, D. A.; Vdovichev, A. A.; Kononov, A. I. Ag−DNA Emitter: Metal Nanorod or Supramolecular Complex? *J. Phys. Chem. Lett.* **2016**, *7*, 3560−3566.

(33) Kilin, D. S.; Prezhdo, O. V.; Xia, Y. N. Shape-Controlled Synthesis of Silver Nanoparticles: Ab Initio Study of Preferential Surface Coordination with Citric Acid. *Chem. Phys. Lett.* **2008**, *458*, 113−116.

(34) Shayeghi, A.; Götz, D. A.; Johnston, R. L.; Schäfer, R. Optical Absorption Spectra and Structures of Ag$_6^+$ and Ag$_8^+$. *Eur. Phys. J. D* **2015**, *69*, 1−5.

(35) Shayeghi, A.; Johnston, R. L.; Schäfer, R. Communication: Global Minimum Search of Ag$_{10}^+$ with Molecular Beam Optical Spectroscopy. *J. Chem. Phys.* **2014**, *141*, 181104.

(36) Bae, G. T.; Aikens, C. M. Time-Dependent Density Functional Theory Studies of Optical Properties of Ag Nanoparticles: Octahedra, Truncated Octahedra, and Icosahedra. *J. Phys. Chem. C* **2012**, *116*, 10356−10367.

(37) Senanayake, R. D.; Akimov, A. V.; Aikens, C. M. Theoretical Investigation of Electron and Nuclear Dynamics in the Au$_{25}$(SH)$_{18}^{(-1)}$ Thiolate-Protected Gold Nanocluster. *J. Phys. Chem. C* **2017**, *121*, 10653−10662.

(38) Goel, S.; Velizhanin, K. A.; Piryatinski, A.; Tretiak, S.; Ivanov, S. A. DFT Study of Ligand Binding to Small Gold Clusters. *J. Phys. Chem. Lett.* **2010**, *1*, 927−931.

(39) Gieseking, R. L.; Ratner, M. A.; Schatz, G. C. Semiempirical Modeling of Ag Nanoclusters: New Parameters for Optical Property Studies Enable Determination of Double Excitation Contributions to Plasmonic Excitation. *J. Phys. Chem. A* **2016**, *120*, 4542−4549.

(40) Kilina, S.; Kilin, D.; Tretiak, S. Light-Driven and Phonon-Assisted Dynamics in Organic and Semiconductor Nanostructures. *Chem. Rev.* **2015**, *115*, 5929−5978.

(41) Rego, L. G. C.; Batista, V. S. Quantum Dynamics Simulations of Interfacial Electron Transfer in Sensitized TiO$_2$ Semiconductors. *J. Am. Chem. Soc.* **2003**, *125*, 7989−7997.

(42) High, J. S.; Rego, L. G. C.; Jakubikova, E. Quantum Dynamics Simulations of Excited State Energy Transfer in a Zinc−Free-Base Porphyrin Dyad. *J. Phys. Chem. A* **2016**, *120*, 8075−8084.

(43) Ben-Nun, M.; Martinez, T. J. Nonadiabatic Molecular Dynamics: Validation of the Multiple Spawning Method for a Multidimensional Problem. *J. Chem. Phys.* **1998**, *108*, 7244−7257.

(44) Tao, H.; Levine, B. G.; Martínez, T. J. Ab Initio Multiple Spawning Dynamics Using Multi-State Second-Order Perturbation Theory. *J. Phys. Chem. A* **2009**, *113*, 13656−13662.

(45) Shu, Y.; Fales, B. S.; Levine, B. G. Defect-Induced Conical Intersections Promote Nonradiative Recombination. *Nano Lett.* **2015**, *15*, 6247.

(46) Tully, J. C. Molecular Dynamics with Electronic Transitions. *J. Chem. Phys.* **1990**, *93*, 1061−1071.

(47) Redfield, A. G. On the Theory of Relaxation Processes. *IBM J. Res. Dev.* **1957**, *1*, 19−31.

(48) Chen, H.; McMahon, J. M.; Ratner, M. A.; Schatz, G. C. Classical Electrodynamics Coupled to Quantum Mechanics for Calculation of Molecular Optical Properties: a RT-TDDFT/FDTD Approach. *J. Phys. Chem. C* **2010**, *114*, 14384−14392.

(49) Neukirch, A. J.; Guo, Z.; Prezhdo, O. V. Time-Domain Ab Initio Study of Phonon-Induced Relaxation of Plasmon Excitations in a Silver Quantum Dot. *J. Phys. Chem. C* **2012**, *116*, 15034−15040.

(50) Long, R.; Prezhdo, O. V. Instantaneous Generation of Charge-Separated State on Tio2 Surface Sensitized with Plasmonic Nanoparticles. *J. Am. Chem. Soc.* **2014**, *136*, 4343−4354.

(51) Kilin, D. S.; Micha, D. A. Relaxation of Photoexcited Electrons at a Nanostructured Si(111) Surface. *J. Phys. Chem. Lett.* **2010**, *1*, 1073−1077.

(52) Huang, S.; Inerbaev, T. M.; Kilin, D. Excited State Dynamics of Ru$_{10}$ Cluster Interfacing Anatase TiO$_2$(101) Surface and Liquid Water. *J. Phys. Chem. Lett.* **2014**, *5*, 2823−2829.

(53) Jensen, S. J.; Inerbaev, T. M.; Kilin, D. S. Spin Unrestricted Excited State Relaxation Study of Vanadium(IV)-Doped Anatase. *J. Phys. Chem. C* **2016**, *120*, 5890−5905.

(54) Jensen, S. J.; Inerbaev, T. M.; Abuova, A. U.; Kilin, D. S. Spin Unrestricted Nonradiative Relaxation Dynamics of Cobalt-Doped Anatase Nanowire. *J. Phys. Chem. C* **2017**, *121*, 16110−16125.

(55) Chen, J.; Schmitz, A.; Inerbaev, T.; Meng, Q.; Kilina, S.; Tretiak, S.; Kilin, D. S. First-Principles Study of p-n Doped Silicon Quantum Dots: Charge Transfer, Energy Dissipation, and Time-Resolved Emission. *J. Phys. Chem. Lett.* **2013**, *4*, 2906−2913.

(56) Vogel, D. J.; Kilin, D. S. First-Principles Treatment of Photoluminescence in Semiconductors. *J. Phys. Chem. C* **2015**, *119*, 27954−27964.

(57) Brown, S. L.; Vogel, D. J.; Miller, J. B.; Inerbaev, T. M.; Anthony, R. J.; Kortshagen, U. R.; Kilin, D. S.; Hobbie, E. K. Enhancing Silicon Nanocrystal Photoluminescence through Temperature and Microstructure. *J. Phys. Chem. C* **2016**, *120*, 18909−18916.

(58) Meng, Q. G.; May, P. S.; Berry, M. T.; Kilin, D. S. Time-Resolved Electronic and Optical Properties of a Thiolate Protected Au38 Nanocluster. *Mol. Phys.* **2015**, *113*, 408−417.

(59) Kohn, W.; Sham, L. J. Self-Consistent Equations Including Exchange and Correlation Effects. *Phys. Rev.* **1965**, *140*, A1133−A1138.

(60) Kaduk, B.; Kowalczyk, T.; Van Voorhis, T. Constrained Density Functional Theory. *Chem. Rev.* **2012**, *112*, 321−370.

(61) Yao, G.; Berry, M. T.; May, P. S.; Kilin, D. DFT Calculation of Russell−Saunders Splitting for Lanthanide Ions Doped in Hexagonal (β)-NaYF$_4$ Nanocrystals. *J. Phys. Chem. C* **2013**, *117*, 17177−17185.

(62) Parr, R. G.; Yang, W. *Density-Functional Theory of Atoms and Molecules*; Oxford University Press: Oxford, U.K., 1994.

(63) Vogel, D. J.; Kryjevski, A.; Inerbaev, T. M.; Kilin, D. S. Photoinduced Single- and Multiple- Electron Dynamics Processes Enhanced by Quantum Confinement in Lead Halide Perovskite Quantum Dots. *J. Phys. Chem. Lett.* **2017**, *8*, 3032.

(64) Kilin, D. S.; Tsemekhman, K.; Prezhdo, O. V.; Zenkevich, E. I.; von Borczyskowski, C. Ab Initio Study of Exciton Transfer Dynamics from a Core-Shell Semiconductor Quantum Dot to a Porphyrin-Sensitizer. *J. Photochem. Photobiol., A* **2007**, *190*, 342−351.

(65) Hammes-Schiffer, S.; Tully, J. C. Proton Transfer in Solution – Molecular Dynamics with Quantum Transitions. *J. Chem. Phys.* **1994**, *101*, 4657−4667.

(66) Shafai, G.; Hong, S. Y.; Bertino, M.; Rahman, T. S. Effect of Ligands on the Geometric and Electronic Structure of Au-13 Clusters. *J. Phys. Chem. C* **2009**, *113*, 12072−12078.

(67) Furche, F.; Ahlrichs, R.; Weis, P.; Jacob, C.; Gilb, S.; Bierweiler, T.; Kappes, M. M. The Structures of Small Gold Cluster Anions as Determined by a Combination of Ion Mobility Measurements and Density Functional Calculations. *J. Chem. Phys.* **2002**, *117*, 6982−6990.

(68) Paulsen, R. T.; Kilin, D. S. Silver Nanoparticles for Catalysis of Hydrogen Peroxide Decomposition: Atomistic Modeling. *MRS Online Proc. Libr.* **2015**, *1787*, 21−25.

(69) Blochl, P. E. Projector Augmented-Wave Method. *Phys. Rev. B: Condens. Matter Mater. Phys.* **1994**, *50*, 17953−17979.

(70) Kresse, G.; Joubert, D. From Ultrasoft Pseudopotentials to the Projector Augmented-Wave Method. *Phys. Rev. B: Condens. Matter Mater. Phys.* **1999**, *59*, 1758−1775.

(71) Perdew, J. P.; Burke, K.; Ernzerhof, M. Generalized Gradient Approximation Made Simple. *Phys. Rev. Lett.* **1996**, *77*, 3865−3868.

(72) Kohn, W.; Sham, L. J. Self-Consistent Equations Including Exchange and Correlation Effects. *Phys. Rev.* **1965**, *140*, A1133.

(73) Heyd, J.; Scuseria, G. E.; Ernzerhof, M. Hybrid Functionals Based on a Screened Coulomb Potential. *J. Chem. Phys.* **2003**, *118*, 8207−8215.

(74) Becke, A. D. Density-Functional Thermochemistry. Iii. The Role of Exact Exchange. *J. Chem. Phys.* **1993**, *98*, 5648−5652.

(75) Lee, C. T.; Yang, W. T.; Parr, R. G. Development of the Colle-Salvetti Correlation-Energy Formula into a Functional of the Electron-Density. *Phys. Rev. B: Condens. Matter Mater. Phys.* **1988**, *37*, 785−789.

(76) Neugebauer, J.; Scheffler, M. Adsorbate-Substrate and Adsorbate-Adsorbate Interactions of Na and K Adlayers on Al(111). *Phys. Rev. B: Condens. Matter Mater. Phys.* **1992**, *46*, 16067−16080.

(77) Makov, G.; Payne, M. C. Periodic Boundary Conditions in Ab Initio Calculations. *Phys. Rev. B: Condens. Matter Mater. Phys.* **1995**, *51*, 4014−4022.

(78) Meng, Q. G.; Chen, J. C.; Kilin, D. Proton Reduction at Surface of Transition Metal Nanocatalysts. *Mol. Simul.* **2015**, *41*, 134−145.

(79) Meng, Q. G.; May, P. S.; Berry, M. T.; Kilin, D. Sequential Hydrogen Dissociation from a Charged Pt$_{13}$H$_{24}$ Cluster Modeled by Ab Initio Molecular Dynamics. *Int. J. Quantum Chem.* **2012**, *112*, 3896−3903.

(80) Dandu, N.; Tretiak, S.; Kilina, S.; Kilin, D. Through Space and through Bridge Channels of Charge Transfer at p-n Nano-Junctions: A DFT Study. *Chem. Phys.* **2016**, *481*, 144−156.

(81) Fischer, S. A.; Crotty, A. M.; Kilina, S. V.; Ivanov, S. A.; Tretiak, S. Passivating Ligand and Solvent Contributions to the Electronic Properties of Semiconductor Nanocrystals. *Nanoscale* **2012**, *4*, 904−914.

(82) Kilina, S.; Ivanov, S.; Tretiak, S. Effect of Surface Ligands on Optical and Electronic Spectra of Semiconductor Nanoclusters. *J. Am. Chem. Soc.* **2009**, *131*, 7717−7726.

(83) Englman, R.; Jortner, J. The Energy Gap Law for Radiationless Transitions in Large Molecules. *Mol. Phys.* **1970**, *18*, 145.

(84) Rysselberghe, P. V. Remarks Concerning the Clausius-Mossotti Law. *J. Phys. Chem.* **1931**, *36*, 1152−1155.

(85) Ball, P. A New Kind of Alchemy. *New Sci.* **2005**, *186*, 30−33.

(86) Knight, W. D.; Clemenger, K.; Deheer, W. A.; Saunders, W. A.; Chou, M. Y.; Cohen, M. L. Electronic Shell Structure and Abundances of Sodium Clusters. *Phys. Rev. Lett.* **1984**, *52*, 2141−2143.

(87) Brown, S. L.; Miller, J. B.; Anthony, R. J.; Kortshagen, U. R.; Kryjevski, A.; Hobbie, E. K. Abrupt Size Partitioning of Multimodal Photoluminescence Relaxation in Monodisperse Silicon Nanocrystals. *ACS Nano* **2017**, *11* (2), 1597−1603.

(88) Vazhappilly, T.; Kilin, D. S.; Micha, D. A. Modeling the surface photovoltage of silicon slabs with varying thickness. *J. Phys.: Condens. Matter* **2015**, *27*, 134204.

DOI: 10.1021/acs.jpcc.7b04870